JBC RESEARCH ARTICLE

A unique aromatic residue modulates the redox range of a periplasmic multiheme cytochrome from *Geobacter metallireducens*

Received for publication, March 12, 2021, and in revised form, April 21, 2021 Published, Papers in Press, April 26, 2021,
https://doi.org/10.1016/j.jbc.2021.100711

Pilar C. Portela, Marta A. Silva, Liliana R. Teixeira, and Carlos A. Salgueiro*

From the UCIBIO-Requimte, Departamento de Química, Faculdade de Ciências e Tecnologia, Universidade NOVA de Lisboa, Campus Caparica, Caparica, Portugal

Edited by F. Peter Guengerich

Geobacter **bacteria are able to transfer electrons to the exterior of the cell and reduce extracellular electron acceptors including toxic/radioactive metals and electrode surfaces, with potential applications in bioremediation or electricity harvesting. The triheme *c*-type cytochrome PpcA from *Geobacter metallireducens* plays a crucial role in bridging the electron transfer from the inner to the outer membrane, ensuring an effective extracellular electron transfer. This cytochrome shares 80% identity with PpcA from *Geobacter sulfurreducens*, but their redox properties are markedly different, thus determining the distinctive working redox potential ranges in the two bacteria. PpcA from *G. metallireducens* possesses two extra aromatic amino acids (Phe-6 and Trp-45) in its hydrophobic heme core, whereas PpcA from *G. sulfurreducens* has a leucine and a methionine in the equivalent positions. Given the different nature of these residues in the two cytochromes, we have hypothesized that the extra aromatic amino acids could be partially responsible for the observed functional differences. In this work, we have replaced Phe-6 and Trp-45 residues by their nonaromatic counterparts in PpcA from *G. sulfurreducens*. Using redox titrations followed by UV–visible and NMR spectroscopy we observed that residue Trp-45 shifted the redox potential range 33% toward that of PpcA from *G. sulfurreducens*, whereas Phe-6 produced a negligible effect. For the first time, it is shown that the inclusion of an aromatic residue at the heme core can modulate the working redox range in abundant periplasmic proteins, paving the way to engineer bacterial strains for optimal microbial bioelectrochemical applications.**

Anaerobic environments are prolific in microbial communities that have developed different strategies to obtain energy without using oxygen as terminal electron acceptor in respiration processes. Dissimilatory metal-reducing organisms, such as the ones belonging to the *Geobacter* genera, couple cellular growth to the reduction of metals present in the environment (1). This is only possible because of the development of an extracellular electron transport chain that is capable of shuttling electrons from the cell's interior to the environment (2). *Geobacter* bacteria typically colonize aquatic sediments, wetlands, rice paddies, and subsurface environments (2) where the concentration of Fe(III) in sediments frequently exceeds that of other electron acceptors, such as oxygen, nitrate, and sulfate (3, 4). This reduction is not only highly advantageous for the bacteria but also plays an essential role in the ecosystem's geochemistry because it releases dissolved Fe(II) and Mn(II) as well as trace metals, metalloids, and phosphate that adsorb onto Fe(III) and Mn(IV) oxides.

The *Geobacter metallireducens* bacterium presents the unique ability of oxidizing an enormous variety of organic compounds both aromatic (such as benzaldehyde, phenol, benzene, and toluene) and nonaromatic (such as butanol, ethanol, and propanol) compared with *Geobacter sulfurreducens*, which is only able to oxidize acetate, formate, lactate, or pyruvate (the latter only when hydrogen is the electron donor) (2, 5). Both species are capable of utilizing Fe(III), Mn(IV), or humic substances as terminal electron acceptors, as well as water contaminants such as U(VI) and Tc(VII) (2). This physiological hallmark has been used for the bioremediation of waters contaminated with these compounds (6–8). However, the biotechnological applications of *Geobacter* are not only circumscribed to the bioremediation of contaminated waters, as their extracellular electron transfer pathways can be used for the sustainable production of electrical current from a wide range of organic wastes in microbial fuel cell devices (9, 10).

To ensure the efficient extracellular electron transfer, *Geobacter* bacteria rely on a complex network of *c*-type cytochromes. In fact, *c*-type cytochromes comprise 2.2% and 2.6% of the genome of *G. metallireducens* and *G. sulfurreducens*, respectively, and more than 86% of these cytochromes possess more than one heme group (11). The cytochromes are distributed along the inner membrane, periplasm, and outer membrane and are responsible for guiding the electron flow from the cytoplasm to the cell's exterior, constituting an excellent target for the improvement of extracellular electron transfer effectiveness (11, 12). The current model for electron transfer in *Geobacter* (Fig. 1) postulates that electrons originating from the oxidation of organic compounds are transferred to a menaquinone pool

* For correspondence: Carlos A. Salgueiro, csalgueiro@fct.unl.pt.

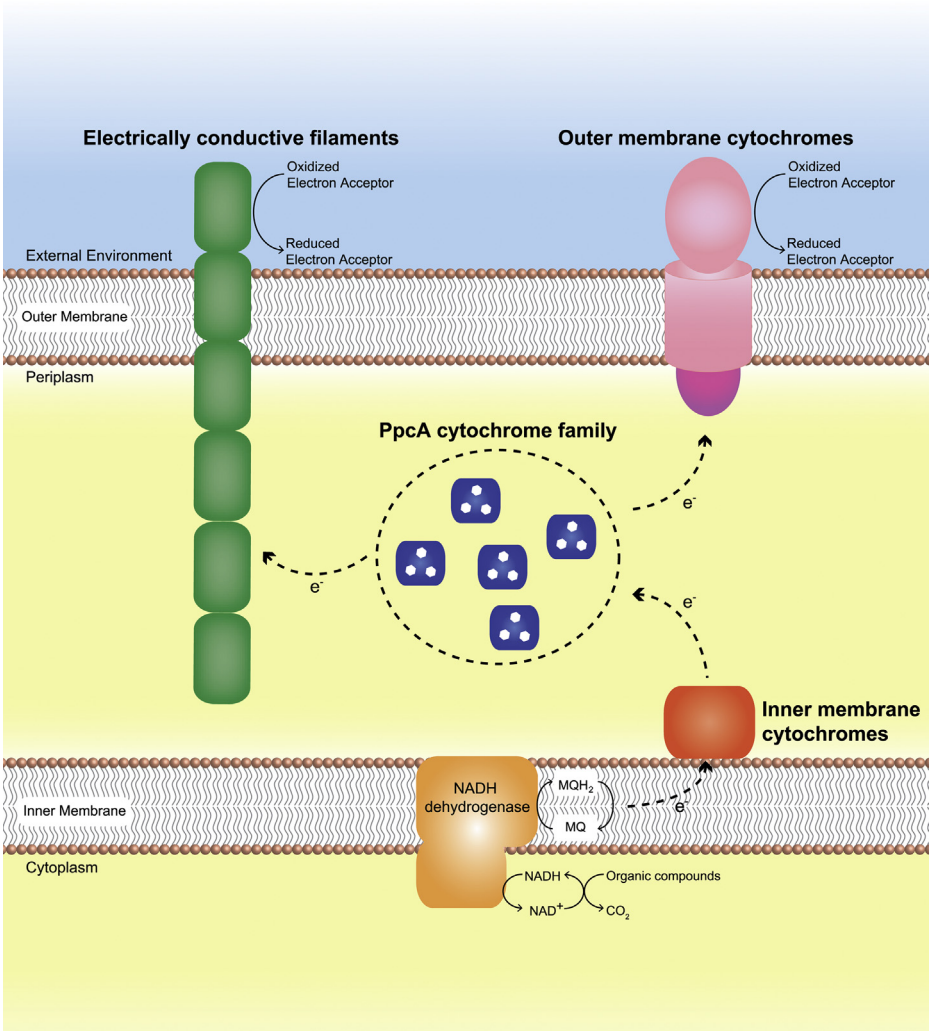

Figure 1. Electron transfer components of the extracellular electron transfer pathway in *Geobacter* bacteria. The NADH dehydrogenase (*orange*) mediates electron transfer from the oxidation of organic compounds to the menaquinone pool (MQ/MQH_2) located in the inner membrane. From there, electrons are transferred to inner membrane–associated cytochromes (*red*), and the PpcA family (*blue*) is responsible for mediating electron transfer from the inner membrane proteins to outer membrane complexes (*pink*). Electrically conductive filaments (*green*), which mediate electron transfer to electrodes, are also depicted. The *white hexagons* represent the heme groups in the PpcA family of cytochromes.

via an NADH dehydrogenase located in the inner membrane (13). Depending on the redox potential of the final electron acceptor, the electrons are transferred to either one of two pathways: the CbcL-dependent pathway, which operates when the final electron acceptors are at or below redox potentials of −100 mV (*versus* the normal hydrogen electrode), whereas the ImcH pathway is used when final electron acceptors are above the referred redox potential (14, 15). The electrons are then transferred from CbcL or ImcH to the PpcA *c*-type cytochrome family located in the periplasm (9), and from these to porin-cytochrome transouter membrane complexes (such as the OmaB–OmbB–OmcB or OmaC–OmbC–OmcC), which convey the electrons to the extracellular electron acceptors (16). In addition to these electron transfer proteins, *Geobacter* bacteria possess electrically conductive filaments (17–19) that establish electrical contacts with electrodes and flagella that allow them to move toward solid extracellular electron acceptors (20).

The PpcA family is composed by triheme cytochromes with negative reduction potentials and bis-histidine axial coordinated hemes (13). To maintain consistency with the literature, the hemes in this family are numbered I, III, and IV, a designation that derives from their superimposition with those of the structurally homologous tetraheme cytochrome c_3 (21). The PpcA family is one of the most conserved among *Geobacter* (11). It is constituted by five cytochromes both in *G. sulfurreducens* and *G. metallireducens*. In *G. sulfurreducens*, the cytochromes are designated PpcA–PpcE, whereas in *G. metallireducens*, they are designated PpcA–PpcF because of the very low degree of homology between the PpcD from *G. sulfurreducens*, and the fifth member from *G. metallireducens*, the designation PpcF was adopted (22).

The cytochrome PpcA from *G. sulfurreducens* has been extensively studied and shares 80% of amino acid sequence identity with PpcA from *G. metallireducens*, differing only in 13 residues. A preliminary structural study has suggested that

these two proteins share a high structural homology with some differences near hemes I and III (23). However, a detailed functional characterization has shown that these two proteins possess markedly different mechanistic properties (24). In fact, the order of oxidation of the heme groups is different (IV–I–III in PpcA from *G. metallireducens* and I–IV–III in PpcA from *G. sulfurreducens*) as well as their apparent midpoint redox potential values (−93 mV for PpcA from *G. metallireducens* and −138 mV for PpcA from *G. sulfurreducens*, at pH 8). Given the high structural similarity between the two cytochromes, their different redox properties, and the fact that PpcA from *G. metallireducens* possesses two extra aromatic amino acids at the heme core (Fig. 2*A*), it was our goal to determine the impact of these two residues in the functional properties of PpcA from *G. metallireducens*. For this, we have replaced the amino acids Phe-6 (F6) and Trp-45 (W45) by their counterparts Leu-6 (L6) and Met-45 (M45) in PpcA from *G. sulfurreducens*. We have constructed two single mutants (PpcAF6L and PpcAW45M) and a double mutant (PpcAF6LW45M) to probe the effect of each single mutation and their joint effect. For each mutant, we first evaluated the structural impact of the mutations using NMR spectroscopy. Then, the effect of the mutations in the midpoint redox potential value was probed by potentiometric titrations followed by UV–visible spectroscopy. For the mutant(s) with the biggest impact on this value, a detailed thermodynamic characterization was obtained using a combination of NMR and UV–visible spectroscopic data. The data obtained allowed us to elucidate the role of the extra aromatic residues in PpcA from *G. metallireducens*, and their contribution to the modulation of the distinct functional properties shown by this cytochrome and its homolog in *G. sulfurreducens*.

Results

Probing the structural impact of the mutations

The structural impact of the introduction of mutations in position 6 or/and 45 was evaluated using NMR spectroscopy. The NMR signals of the side chain's aromatic protons cover a very typical region in the ^{1}H-NMR spectrum and, upon successful introduction of the mutations, the side-chain signals of the replaced aromatic amino acids were no longer observable in the 1D ^{1}H NMR spectra (Fig. 2). This was further corroborated in the 2D ^{1}H and ^{15}N-heteronuclear single quantum coherence (HSQC) spectra in which the characteristic signal $H_{\varepsilon 1}$ from Trp-45 at 10.2 ppm was absent in the PpcAW45M and PpcAF6LW45M mutants but present in the PpcAF6L mutant (Fig. 3).

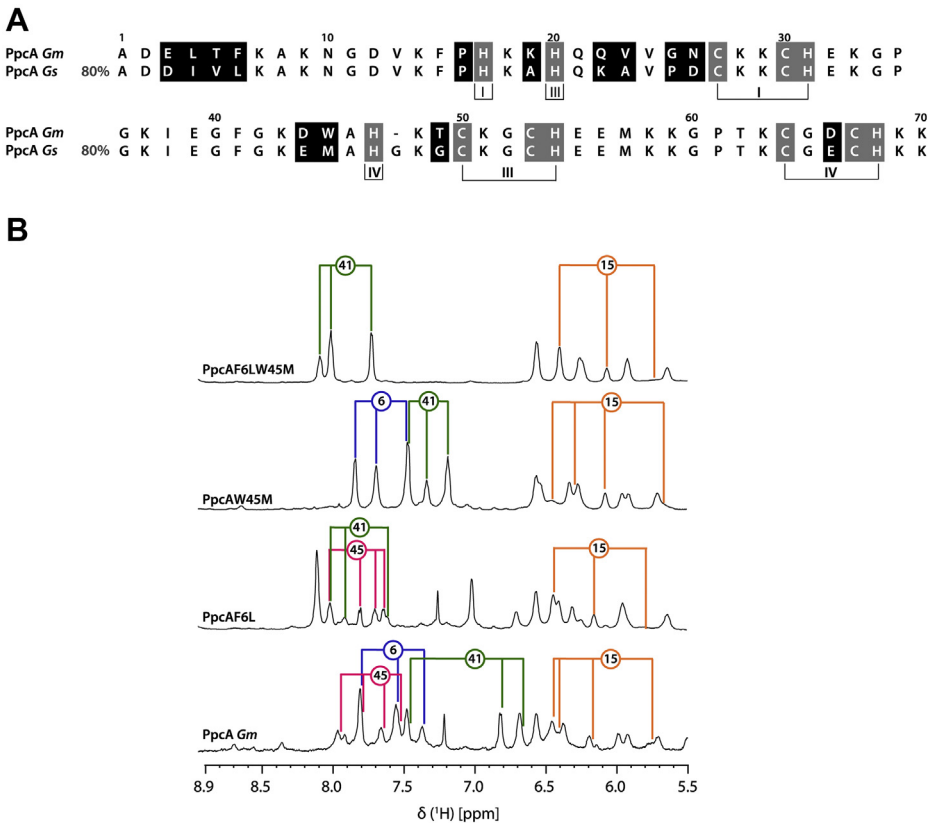

Figure 2. Mutagenesis of residues Phe-6 and Trp-45 in PpcA from *Geobacter metallireducens*. *A*, alignment of the amino acid sequences of the PpcA triheme cytochromes from *G. metallireducens* (*Gm*) and *G. sulfurreducens* (*Gs*). The *black* and *gray boxes* highlight the nonconserved residues and heme-attached residues, respectively. The heme numbering and respective attached residues are indicated at the *bottom* of the last cytochrome amino acid sequence. The percentage of sequence identity relative to PpcA from *G. metallireducens* obtained from the BLAST (30) is indicated. *B*, expansion of the aromatic region in the 1D ^{1}H NMR spectra of wildtype PpcA from *G. metallireducens* (PpcA *Gm*) and its mutants PpcAF6L, PpcAW45M, and PpcAF6LW45M. The chemical shift differences observed for the aromatic protons of the same residue, particularly to those of Phe-41, result from the elimination of the ring-current shifts of the replaced aromatic neighbors (Phe-6 and/or Trp-45).

After confirming the successful replacements of the targeted amino acids, we proceeded to assign the heme substituent and backbone signals of each mutant using, respectively, 2D ^{1}H, ^{1}H-TOCSY, 2D ^{1}H, ^{1}H-NOESY spectra, and 2D ^{1}H, ^{1}H-TOCSY, 2D ^{1}H, ^{1}H-NOESY, and 2D ^{1}H, ^{15}N-HSQC spectra. The assigned signals were deposited in the Biological Magnetic Resonance Data Bank under the accession numbers 50730 (PpcAF6L), 50731 (PpcAW45M), and 50732 (PpcAF6LW45M).

The signal dispersion in the 2D ^{1}H, ^{15}N-HSQC spectra of the mutants is very similar to that of the wildtype protein (Fig. 3). The most affected NH signals are Glu-3 to Ala-8 and Ile-38 to Gly-52 in PpcAF6L and PpcAW45M, respectively (Fig. 3, *A* and *B*). In the double-mutant PpcAF6LW45M, the most affected regions are a combination of the most affected ones in the single mutants (Fig. 3*C*).

We further analyzed the effects of the mutations on the heme substituent signals (Fig. 4). Compared with the wildtype protein, the rmsds of the mutants are low: 0.05, 0.08 and 0.10 ppm for PpcAF6L, PpcAW45M, and PpcAF6LW45M, respectively, although slightly higher for the double mutant, as expected from the substitution of two aromatic rings and elimination of their ring-current effect contribution to the observed chemical shifts. The good correlation obtained for the chemical shifts of heme protons in the mutant and wildtype cytochromes (Fig. 4*A*) indicates that the heme cores were unaffected by the mutations. In PpcAF6L, the most affected substituents are $12^{1}CH_3^{I}$, $12^{1}CH_3^{IV}$, and $2^{1}CH_3^{III}$ (Fig. 4, *B* and *C*). In PpcAW45M, the most affected substituent is $3^{2}CH_3^{III}$, followed by $10H^{I}$, $3^{1}H^{III}$, $8^{1}H^{I}$, $12^{1}CH_3^{I}$, and $12^{1}CH_3^{IV}$. Finally, in PpcAF6LW45M, the most affected substituents are a combination of the most affected ones in the single mutants:

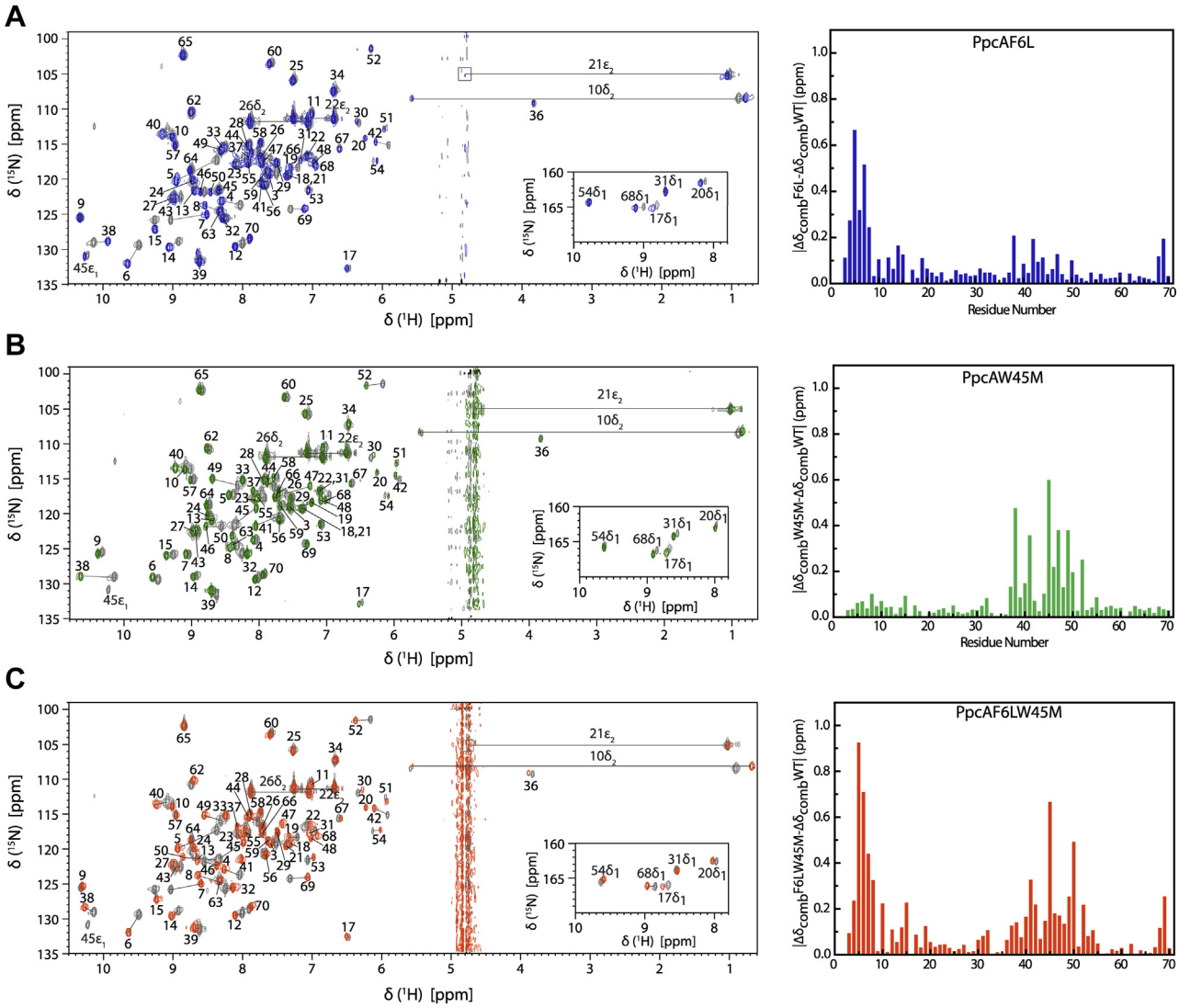

Figure 3. Impact of the F6L, W45M, and F6LW45M mutations on the backbone signals. Comparison between the ^{1}H, ^{15}N-HSQC spectrum of fully reduced mutants—PpcAF6L (*blue contours*—panel *A*), PpcAW45M (*green contours*—panel *B*), or PpcAF6LW45M (*orange contours*—panel *C*)—and wildtype cytochrome (*gray contours*). The most affected signals are connected by a *straight line*. The differences between the combined ^{1}H and ^{15}N chemical shifts observed for the mutants and wildtype cytochrome ($\Delta\delta_{comb}$) are also represented. The combined chemical shift differences were calculated using the equation $\Delta\delta_{comb} = [(\Delta\delta H)^2 + w_i (\Delta\delta N)^2]^{1/2}$, where $\Delta\delta H$ is the difference between ^{1}H shifts, $\Delta\delta N$ the difference between ^{15}N shifts, and $w_i = |\gamma\ ^{15}N\ |/|\gamma\ ^{1}H|$ is a weighting factor that accounts for the differences in nuclei sensitivity (31). HSQC, heteronuclear single quantum coherence.

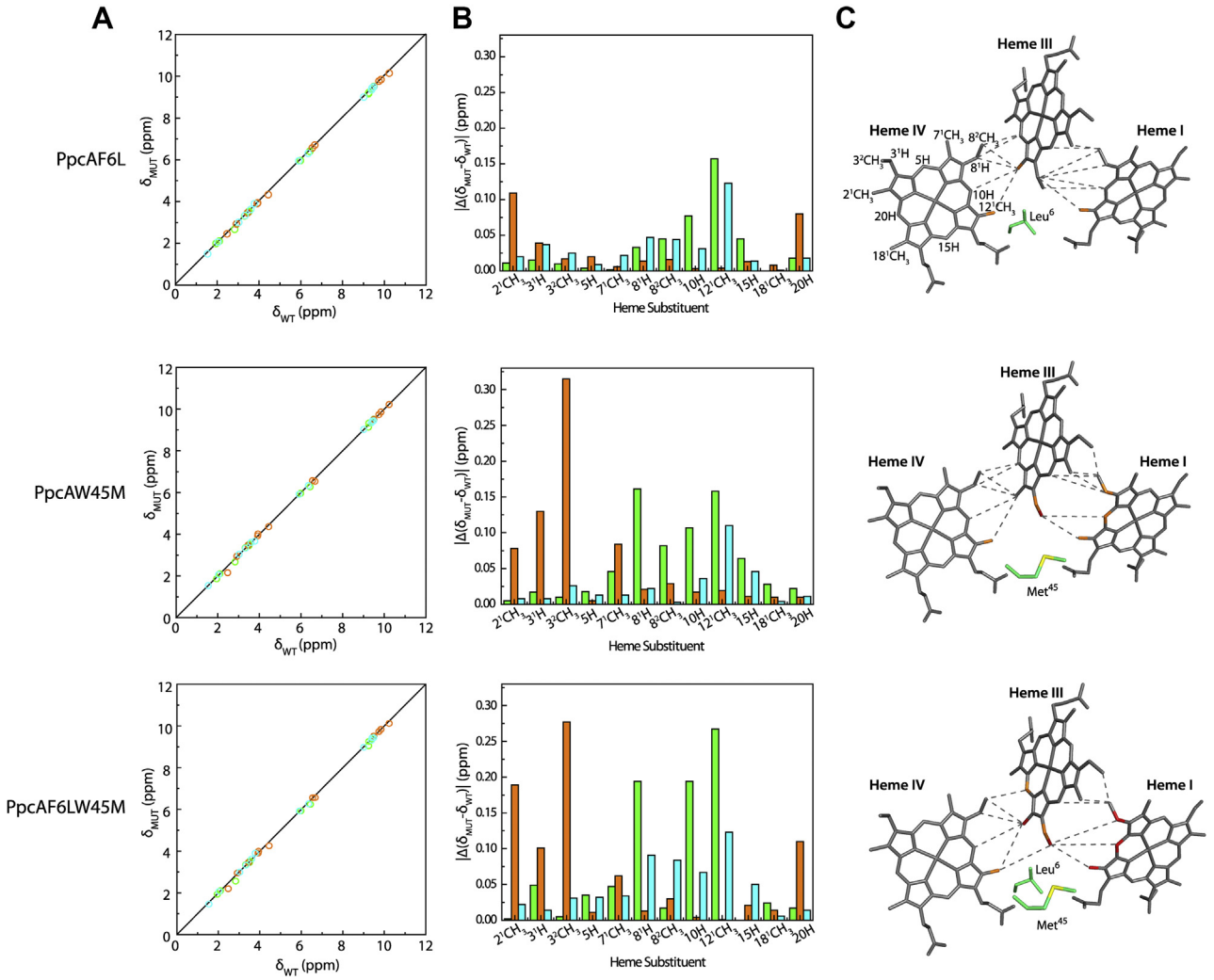

Figure 4. Impact of the F6L, W45M, and F6LW45M mutations on the heme core architecture. *A*, comparison of the heme proton chemical shifts of the PpcA mutants (δ_{MUT}) and those of wildtype (δ_{WT}). *Green*, *orange*, and *blue* symbols correspond to hemes I, III, and IV, respectively. *B*, variation of the heme proton chemical shifts between the mutants' heme substituents (δ_{MUT}) and those of the wildtype (δ_{WT}). The *green*, *orange*, and *blue bars* correspond to hemes I, III, and IV, respectively. *C*, structural location of the most affected substituents and the observed interheme NOE connectivities. The carbon atoms bonded to the affected protons are colored accordingly to the extent to which the substituents are affected: *red* ($\Delta > 0.17$ ppm) and *orange* (0.17 ppm $> \Delta > 0.10$ ppm).

$2^1CH_3^{III}$, $3^2CH_3^{III}$, 8^1H^I, $10H^I$, and $12^1CH_3^I$ are the most affected, followed by 3^1H^{III}, $12^1CH_3^{IV}$, and $20H^{III}$.

Impact of residues Phe-6 and Trp-45 in the global redox properties of PpcA

After confirming that the overall folding and heme core were conserved in the mutated cytochromes, the functional impact of each substitution was probed by determining their apparent redox potential value (E_{app}) through potentiometric titrations followed by UV–visible spectroscopy (Fig. 5). This permitted us to screen the effect of the substitutions on the overall (also designated macroscopic) redox behavior of the proteins and to select the mutants for a redox characterization at the microscopic level to determine the redox properties associated with each redox center. Indeed, the redox curves depicted in Figure 5 only describe the macroscopic redox behavior of the proteins and, in the case of triheme cytochromes, three consecutive one-electron transfer steps convert the fully reduced state in the fully oxidized state (see Experimental procedures section and Fig. S1). Thus, in simple terms, from these redox curves, we can obtain qualitative information about the hemes that dominate the electron transfer in each oxidation step.

The E_{app} values correspond to the point at which the oxidized and reduced fractions of the cytochromes are equal and are listed in Table 1. To better illustrate the effect of the replacements on the redox curves, the fitting of the potentiometric redox titrations of the three mutated proteins is compared with those previously obtained for PpcA cytochromes from *G. metallireducens* and *G. sulfurreducens* in Figure 5 (*bottom-right panel*). The shape of the curve and the E_{app} value of PpcAF6L are similar to the wildtype cytochrome (−90 and −93 mV, respectively). This suggests that the residue Phe-6 has a negligible impact in the modulation of the redox potential of the hemes and, hence, on the less negative working

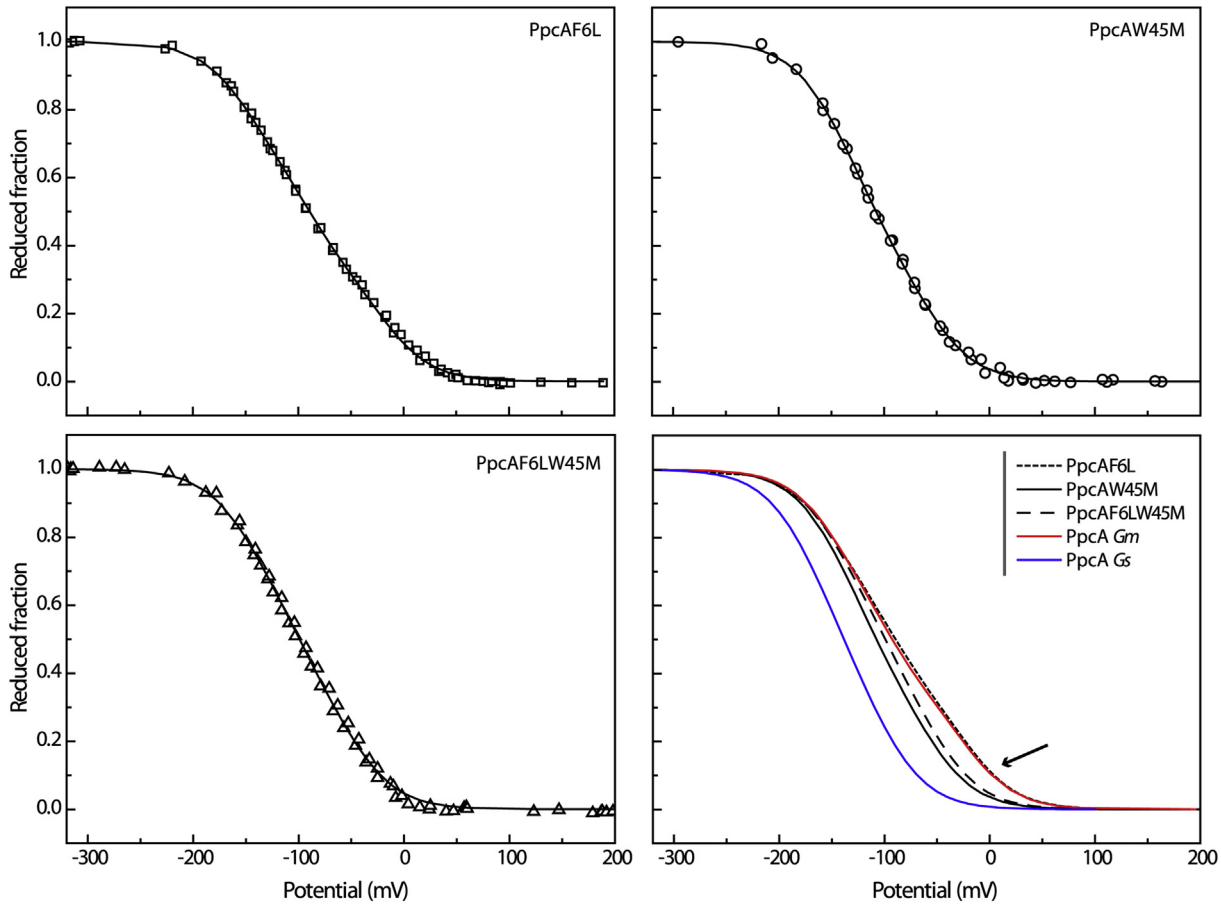

Figure 5. Redox titrations followed by UV–visible spectroscopy for PpcAF6L (*squares*), PpcAW45M (*circles*), and PpcAF6LW45M (*triangles*) at pH 8, 15 °C. The *solid lines* indicate the fitting of the experimental data to a Nernst equation considering three redox centers. The apparent macroscopic redox potential (E_{app}) and the macroscopic redox potentials corresponding to the first (E_1), second (E_2), and third (E_3) oxidation steps are indicated in Table 1. The *bottom-right panel* depicts a comparison of the Nernst fitting of all mutants and wildtype PpcA from *Geobacter metallireducens* (*Gm*) and *G. sulfurreducens* (*Gs*).

potential range of PpcA from *G. metallireducens* compared with its homolog in *G. sulfurreducens*. On the contrary, both the shape and the E_{app} value of PpcAW45M differ substantially from the wildtype cytochrome. The more negative E_{app} value observed for PpcAW45M (−108 mV) clearly indicates that the residue Trp-45 contributes to the less negative E_{app} value of PpcA from *G. metallireducens*. This is further corroborated by the analysis of the double mutant's redox curve, which has a comparable shape to that of PpcAW45M but an E_{app} value (−99 mV) between those of the single mutants PpcAW45M (−108 mV) and PpcAF6L (−90 mV), indicating that the observed effect of the two mutations is additive.

Table 1
Apparent and macroscopic reduction potentials (*versus* normal hydrogen electrode) for mutants PpcAF6L, PpcAW45M, and PpcAF6LW45M at pH 8, 15 °C

Protein	E_{app} (mV)	E_1 (mV)	E_2 (mV)	E_3 (mV)
PpcAF6L	−90 (3)	−152 (3)	−91 (3)	−18 (3)
PpcAW45M	−108 (1)	−155 (1)	−110 (1)	−53 (1)
PpcAF6LW45M	−99 (1)	−151 (1)	−100 (1)	−46 (1)
PpcA *Gm* (23)	−93 (4)	−150 (4)	−95 (4)	−20 (4)
PpcA *Gs* (26)	−138 (5)	−182 (5)	−139 (5)	−93 (5)

The apparent reduction potentials (E_{app}) correspond to the point at which the oxidized and reduced fractions are equal. E_1, E_2, and E_3 are the macroscopic reduction potentials for the first, second, and third oxidation steps, respectively (Fig. S1). Standard errors are indicated in parenthesis. The values for PpcA from *G. metallireducens* (*Gm*) and PpcA from *G. sulfurreducens* (*Gs*) were previously determined and are included for comparison.

Thermodynamic characterization of redox centers in PpcAW45M

Compared with the wildtype cytochrome, the macroscopic redox behavior of the PpcAW45M was the most distinct and shifted by 33% the working redox potential range of the protein toward the one observed for PpcA from *G. sulfurreducens* (Table 1). For this reason, this mutant was selected for a detailed thermodynamic characterization in experimental conditions that match those previously reported for the wildtype protein (24). Therefore, the same set of heme methyl groups ($2^1CH_3^I$, $12^1CH_3^{III}$, and $2^1CH_3^{IV}$) was used to probe the individual heme oxidation profiles in 2D ^{1}H, ^{1}H-EXchange SpectroscopY (EXSY) NMR spectra acquired in the pH range of 6.1 to 8.5. We were able to obtain well-resolved 2D ^{1}H, ^{1}H-EXSY NMR spectra in the indicated pH range, which permitted us to obtain discrete NMR signals for all oxidation stages. As an example, the oxidation profiles of the hemes at pH 6.1 and the correspondent oxidation fraction in each oxidation stage, together with those of the wildtype

protein, are illustrated in Figure 6. The heme oxidation fractions show that heme IV dominates the first oxidation step (52%), followed by heme I in the second (47%) and then by heme III in the third (60%). Compared with the wildtype protein, the oxidation fractions of heme III are the most affected ones (*cf. solid and dashed lines* in Fig. 6*B*). The higher oxidation fraction values of heme III in the mutant suggest that the reduction potential of this heme is decreased. Compared with heme III, the oxidation fractions of the other hemes also vary, though in a lesser extent. These changes occur to compensate the variation of oxidation fractions of heme III since in oxidation stages 1 and 2 only a total of one and two hemes can be oxidized, respectively. The analysis of the slopes of the lines connecting each stage of oxidation in Figure 6*B* also provides the order of oxidation of the heme groups. In fact, and despite the changes in the hemes' oxidation profiles, the oxidation of hemes IV, I, and III dominate the first, second, and third stages of oxidation, respectively, and thus the heme oxidation order is conserved in the mutant and wildtype cytochromes: IV–I–III.

To quantify the variation of the redox centers' thermodynamic parameters in PpcAW45M, the pH dependence of the heme methyl NMR signals, measured at different oxidation stages together with UV–visible redox titration data, was fitted to the thermodynamic model summarized in the Experimental procedures section (Fig. 7). The thermodynamic parameters and macroscopic pK_a values of the redox–Bohr center are indicated in Tables 2 and 3, respectively. As indicated in Figure 7, the data obtained from the NMR and UV–visible potentiometric redox titrations are well described by the thermodynamic model.

Discussion

The introduction of mutations maintains the global fold of the mutant proteins

In the present work, the aromatic residues at position 6 (F6) and 45 (W45) in PpcA from *G. metallireducens* were replaced by the counterparts in PpcA from *G. sulfurreducens* (L6 and M45, respectively—see Fig. 2*A*). NMR spectroscopy is a sensitive technique to probe conformational changes caused by the replacement of residues in proteins. This is particularly notorious in the case of small low-spin triheme cytochromes, as it is the case of PpcA from *G. metallireducens*. In fact, the relatively small number of amino acid residues per heme group yielded well-resolved NMR spectra, which permitted us to evaluate the impact of the replacements in the cytochrome's heme core and polypeptide chain. For all mutants, the introduction of the mutation produced an alteration in the backbone signals of the amino acids located in the vicinity of the mutations (Fig. 3). In the case of PpcAF6LW45M, the most affected backbone signals are a combination of the most affected ones of each of the two single mutants.

Concerning the heme core, the good correlation obtained for the chemical shifts of heme protons in the mutant and wildtype cytochromes (Fig. 4) indicates that the heme cores were unaffected by the mutations. In fact, the signals are only marginally affected in the three mutants. The rmsd value of PpcAF6LW45M (0.10 ppm) is slightly higher in comparison with the other values of the mutants since there was substitution of two aromatic rings and elimination of their ring-current effect contribution to the observed chemical shifts.

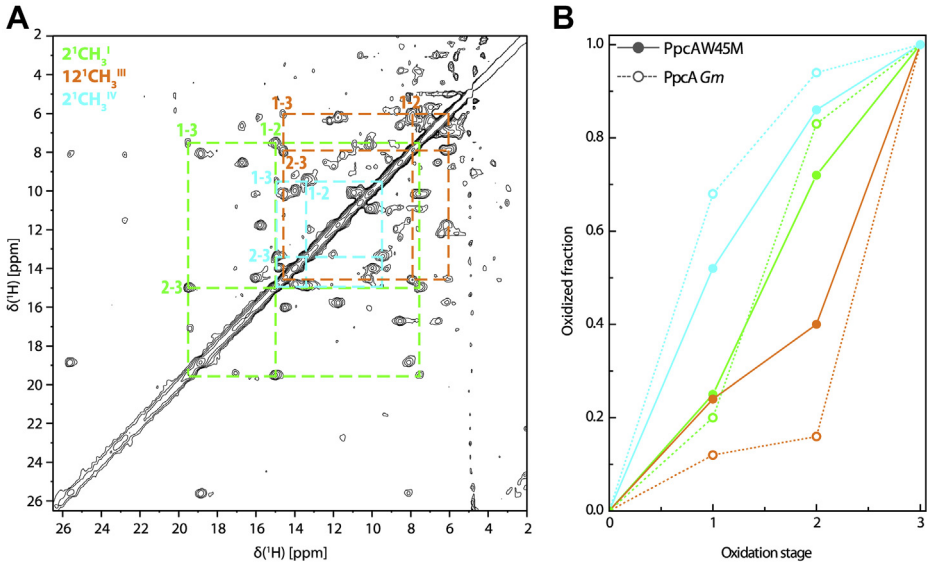

Figure 6. Heme oxidation profile of PpcAW45M. *A*, expansion of 2D ^{1}H, ^{1}H-EXSY NMR spectrum of PpcAW45M obtained at 15 °C, pH 6.1. The *crosspeaks* that result from intermolecular electron transfer between the oxidation stages 1 to 3 are indicated, and connected by *dashed lines*, for the heme methyls $2^{1}CH_3^{I}$ (*green*), $12^{1}CH_3^{III}$ (*orange*), and $2^{1}CH_3^{IV}$ (*blue*). Roman (I, III, and IV) and Arabic (1, 2 and 3) numbers indicate the heme number and the oxidation stages, respectively. The *crosspeaks* to oxidation stage 0 are not shown to not overcrowd the figure. *B*, comparison of the oxidation fractions of PpcAW45M (*solid symbols* and *lines*) and PpcA from *Geobacter metallireducens* (*Gm*) (*open symbols* and *dashed lines*). The oxidation fractions of hemes I, III, and IV are colored *green*, *orange*, and *blue*, respectively. The heme oxidation fractions were calculated according to the equation $x_i = (\delta_i - \delta_0)/(\delta_3 - \delta_0)$, where δ_i, δ_0, and δ_3 are the observed chemical shifts of each methyl in stages *i*, *0*, and *3*, respectively. EXSY, EXchange SpectroscopY.

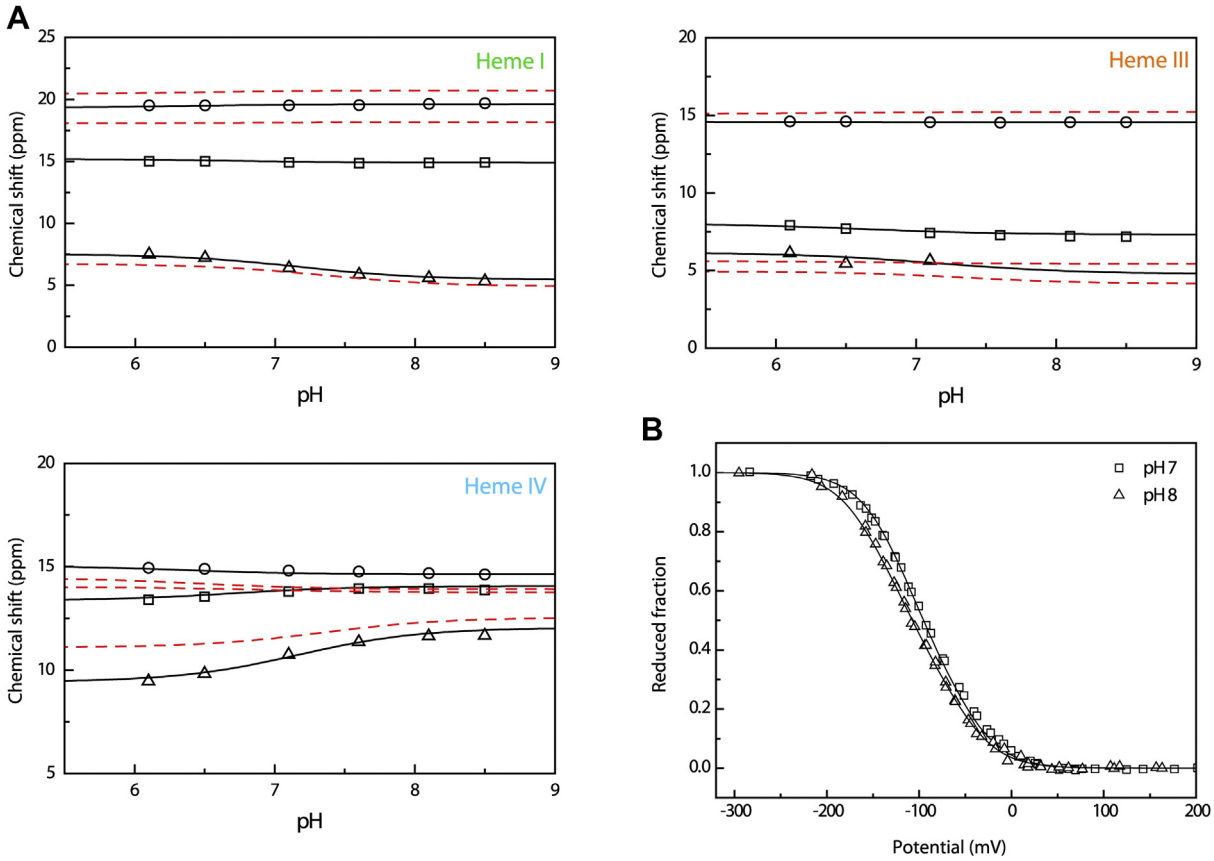

Figure 7. Fitting of the thermodynamic model to the experimental data for PpcAW45M. The *black solid lines* represent the simultaneous fitting of the NMR (*A*) and UV–visible data (*B*), and the *red dashed lines* indicate the fitting for the wildtype protein (24). Panel *A* depicts the variation of the heme methyl chemical shifts at oxidation stages 1 (*triangles*), 2 (*squares*), and 3 (*circles*). The chemical shift of heme methyls in the fully reduced state is not plotted since they are unaffected by the pH. Panel *B* depicts the redox titrations followed by UV–visible spectroscopy for PpcAW45M at pH 7 (*squares*) and pH 8 (*triangles*).

In all mutants, the most affected signals correspond to the substituents facing the hydrophobic core of the protein, which have NOE connectivities with the mutated residues in the wildtype protein (Fig. 4, *B* and *C*). It is worth noting that, for both single mutants, the differences between the wildtype and the mutants' chemical shifts are of the same magnitude (with exception of $3^2CH_3^{III}$ substituent in W45M), which indicates that the mutations have a comparable impact in the heme substituent chemical shifts. In the double mutant, the differences between the wildtype and the mutant's chemical shifts are slightly higher because of the simultaneous removal of two aromatic amino acids.

Table 2
Thermodynamic parameters determined for PpcAW45M in the fully reduced and protonated form

	Energy (meV)			
Protein's redox centers	**Heme I**	**Heme III**	**Heme IV**	**Redox–Bohr center**
PpcAW45M (this work)				
Heme I	**−95 (4)**	23 (2)	7 (3)	−19 (6)
Heme III		**−94(4)**	26 (3)	−19 (6)
Heme IV			**−112 (4)**	−47 (6)
Redox–Bohr center				**447 (8)**
PpcA *Gm* (24)				
Heme I	**−80 (6)**	35 (4)	3 (5)	−22 (6)
Heme III		**−70 (7)**	37 (7)	−23 (7)
Heme IV			**−113 (6)**	−49 (6)
Redox–Bohr center				**463 (13)**
PpcA *Gs* (32)				
Heme I	**−154 (5)**	27 (2)	16 (3)	−32 (4)
Heme III		**−138 (5)**	41 (3)	−31 (4)
Heme IV			**−125 (5)**	−58 (4)
Redox–Bohr center				**495 (8)**

All energies are reported in mili electronvolt, with standard errors given in parentheses. The diagonal energy parameters in bold correspond to the oxidation energies of the hemes and the deprotonating energy of the redox–Bohr center. The off-diagonal energy values correspond to the redox (heme–heme) and redox–Bohr (heme–proton) interaction energies. The thermodynamic parameters of wildtype PpcA from *G. metallireducens* (*Gm*) and of PpcA from *G. sulfurreducens* (*Gs*) are also indicated for comparison.

Table 3
Macroscopic pK_a values of the redox–Bohr center in PpcAW45M mutant from *Geobacter metallireducens*

Protein	Oxidation stage				ΔpK_a
	0	1	2	3	
PpcAW45M (this work)	7.8	7.2	6.7	6.3	1.5
PpcA *Gm* (24)	8.1	7.3	6.9	6.5	1.6
PpcA *Gs* (32)	8.6	8.0	7.2	6.5	2.1

The values were calculated with the parameters presented in Table 2. For comparison, the macroscopic pK_a values of the cytochromes PpcA from *G. metallireducens* (*Gm*) and PpcA from *G. sulfurreducens* (*Gs*) are also indicated.

Trp-45 is a key regulator of the redox properties of PpcA

The initial screening of the impact of the mutations on the overall or macroscopic redox behavior of each mutant indicated that residues 6 and 45 have opposite effects in the modulation of the redox properties of PpcA from *G. metallireducens* and that, in the case of a double mutation, their effect is additive (Table 1 and Fig. 5). In the case of PpcAF6L, the redox curve is similar to the one obtained for the wildtype cytochrome, though shifted to slightly higher redox potential values. On the contrary, PpcAW45M and PpcAF6LW45M mutants have their redox curves shifted to more negative values. In addition, the mutants' curves are steeper compared with the wildtype, particularly in the last third of oxidation, at higher redox potential values, a region that is essentially dominated by the oxidation of the heme with the highest redox potential value (see the *arrow* in Fig. 5). Therefore, from the analysis of the macroscopic redox curves, it can be predicted that the redox potential values of the hemes are more negative but less separated compared with the wildtype cytochrome. Since the more pronounced effects were observed for PpcAW45M, this mutant was selected to test these hypotheses. To attain this, a thermodynamic characterization at the microscopic level of the PpcAW45M mutant was pursued, including the determination of the reduction potential values of the individual hemes and their redox and redox–Bohr interactions.

The thermodynamic parameters obtained for PpcAW45M are listed in Table 2 and show that in the fully reduced and protonated form, just like in the wildtype protein, the redox potentials of the hemes in PpcAW45M are all negative and different from each other. In addition, the redox interactions between each pair of hemes are positive, indicating that the oxidation of a particular heme stabilizes the reduced form of its neighbor. The strongest redox interactions are observed between the hemes that are closer in proximity: I–III and III–IV. However, and despite this apparent conservation of the redox properties in the mutant and wildtype cytochromes, the values clearly show that the redox potential of heme III, followed by that of heme I, are considerably more negative in the mutant, whereas that of heme IV is essentially unaltered. These results are in line with the spatial location of Trp-45 near hemes I and III.

The redox–Bohr interactions between the hemes and the redox–Bohr center are negative, which means the oxidation of the hemes facilitates the deprotonation of the acid–base center and vice versa. The highest redox–Bohr interaction value is observed for heme IV, similarly to the wildtype protein, indicating that the mutation does not impact the redox–Bohr center and its interactions' network. This is also corroborated by the pK_a values determined for the redox–Bohr center in the different oxidation stages (Table 3). In fact, the pK_a values cover a similar region, and the total redox–Bohr effect is essentially the same (1.5 and 1.6 pH units for PpcAW45M and wildtype protein, respectively).

Effect of the mutation on the cytochrome's functional mechanism at physiological pH

From the thermodynamic values indicated in Table 2, it is now possible to evaluate the functional mechanism of PpcAW45M at physiological pH, including (i) the profile of the oxidation curve for each individual heme, which directly provides their redox potential values and order of oxidation as well as (ii) the relative contribution of each microstate during the oxidation (Fig. 8). It is important to stress that, because the individual heme redox potential values are modulated both by redox interactions and redox–Bohr interactions, the potentials at pH 7 differ from those observed for the fully reduced and protonated protein (reported in Table 2). The data obtained showed that the redox potential values of the hemes cover a smaller range (−123 to −67 mV) compared with the wildtype cytochrome (−121 to −18 mV) (Fig. 8, *upper panels*). A comparison of the microscopic reduction potential values (e_{app}) of PpcAW45M and the wildtype protein shows that the reduction potential of heme IV is essentially unaltered (−123 *versus* −121 mV in the mutant and wildtype, respectively), whereas the reduction potential values of hemes I and III are decreased by 11 and 49 mV, respectively (Fig. 8, *upper panel*). The narrow range observed for the mutant is then explained by the significant decrease of the redox potential value of heme III (−67 *versus* −18 mV in the wildtype). Despite these significant changes in the overall oxidation profiles, the order of oxidation of the hemes is conserved: IV–I–III (Fig. 8). However, this does not imply that the functional mechanism of the protein is also conserved, since important changes were observed in the redox properties of hemes I and III. The functional mechanism of the mutant can be evaluated by determining the relative contribution of each of the 16 possible microstates along the redox cycle of the protein (Fig. S1). A well-defined electron pathway is favored when one microstate clearly contributes (highest molar fraction) over that of another microstate within the same oxidation stage, thus favoring the directionality of electron transfer. In the wildtype cytochrome (Fig. 8), due to the considerable separation of the heme redox potential values, the microstate with heme IV oxidized (P_{4H}) will dominate the first oxidation stage (S_1), followed by the microstate with both hemes IV and I oxidized (P_{14}) in the second oxidation stage (S_2) and finally by the oxidation of heme III (P_{134}). Thus, a well-defined preferential electron transfer pathway is established: $P_{0H} \rightarrow P_{4H} \rightarrow P_{14} \rightarrow P_{134}$ (Fig. 8, *lower panel*). This pathway is no longer observed in PpcAW45M (Fig. 8, *lower panel*). In fact, because of the

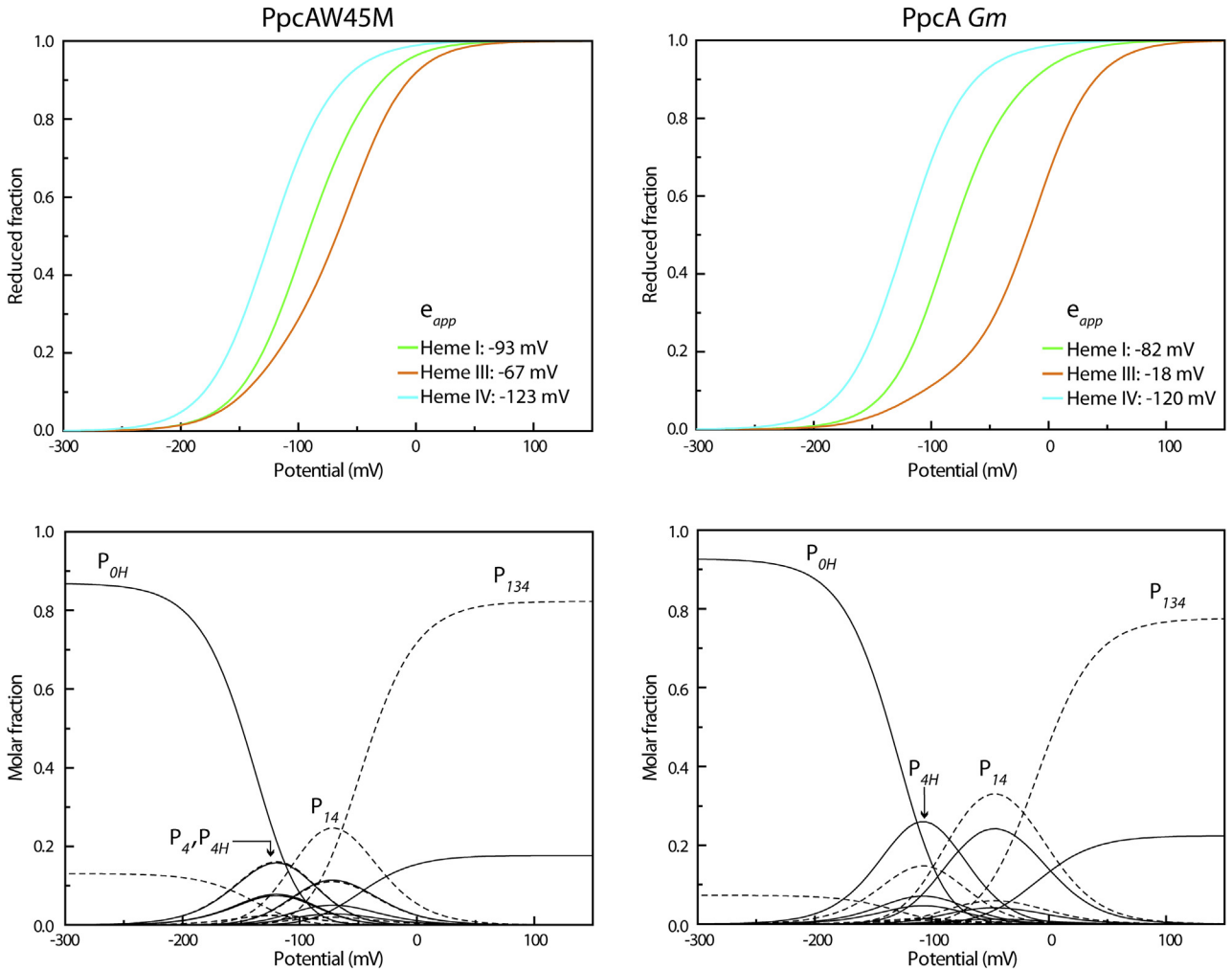

Figure 8. Effect of the Trp-45 mutation in the microscopic properties of PpcA at pH 7. The *upper panel* shows the individual heme oxidation profiles for both the PpcAW45M mutant and wildtype cytochromes. The *green*, *orange*, and *blue curves* correspond, respectively, to hemes I, III, and IV. The curves were calculated as a function of the solution potential using the parameters indicated in Table 2. The midpoint reduction potentials (e_{app}) of the individual hemes are also indicated. The *lower panel* shows the molar fractions of the 16 individual microstates of PpcAW45M mutant and wildtype cytochromes. The *curves* were also calculated as a function of the solution potential using the parameters indicated in Table 2. The protonated and deprotonated microstates are depicted in *solid* and *dashed lines*, respectively (Fig. S1). To not overcrowd the figure, only the relevant microstates are labeled.

decrease of the redox potential values of hemes III and I, the contribution of the microstates with these hemes oxidized in the oxidation stage 1 is higher compared with the wildtype protein. Consequently, the fractional contribution of the dominant microstate P_{4H} is much lower in the mutant and equals that of the microstate P_4 (Fig. 8, *lower panel*). Thus, the preferred pathway observed for the wildtype protein is no longer observed in the mutated protein. Thus, the data obtained clearly indicate that the tryptophan residue at position 45 plays a crucial role in the regulation of the working redox potential range of PpcA and in the maintenance of a well-defined electron transfer pathway.

Conclusions and implications

Electrochemical measurements on naturally grown biofilms of *G. sulfurreducens*' cells on electrode surfaces showed an optimal electron transfer to the electrode at −0.15 V (25). This potential was correlated with the working redox potential range of the abundant periplasmic PpcA cytochrome (26), establishing this cytochrome as one of the main targets for the control of the working redox potential range in *Geobacter* cells. This is particularly useful as one of the means for improving *Geobacter*-based microbial bioelectrochemical applications in which a fine tuning of the redox properties of the electron transfer proteins can be explored. The markedly different functional properties of PpcA from *G. metallireducens* and PpcA from *G. sulfurreducens* are striking when considering that these proteins only differ in 13 amino acids, constituting a useful model for testing the impact of specific residues in their overall redox behavior. We investigated the role of Phe-6 and Trp-45 in the modulation of the functional properties of PpcA from *G. metallireducens* by replacing these amino acids by their counterparts in PpcA from *G. sulfurreducens*—Leu-6 and Met-45. We constructed two single mutants—PpcAF6L and PpcAW45M—and a double mutant—PpcAF6LW45M—and confirmed by NMR that

the mutations did not introduce significant structural modifications. The impact of the mutations in the macroscopic redox behavior of the protein was probed by redox titrations followed by UV–visible spectroscopy, showing that only PpcAW45M produced a marked alteration in the redox profile of the protein to more negative heme redox potentials in comparison with the wildtype protein. A full thermodynamic characterization of the PpcAW45M mutant showed that Trp-45 is determinant in the modulation of the redox properties of heme III and, in less extent, heme I. This study provides a better understanding on the fundamental factors that modulate the redox properties of cytochromes with a pivotal role in *Geobacter*'s electron transfer chain, setting the stage for the rational engineering of cytochromes with specific working redox potential windows. Consequently, the design of periplasmic proteins with enhanced electron transfer driving force from upstream or downstream partners will contribute to the creation of *Geobacter* cells with improved electron transfer capabilities. Overall, this work highlights the key role played by a specific aromatic residue in the modulation of the redox properties of highly abundant and homolog periplasmic cytochromes, offering new directions for the rational modulation and tuning of the electron transfer flow in *Geobacter*.

Experimental procedures

Mutagenesis of residues Phe-6 and Trp-45

The primers responsible for the substitution of residues Phe-6 (F6) and Trp-45 (W45) were designed by the QuikChange Primer Design program (Agilent Technologies) and synthesized by Invitrogen. For the F6L mutation, the primers used were 5'-CCGCTGACGAGCTTACCTTAAAGGCAAAGAACG-3'/5'-CGTTCTTTGCCTTTAAGGTAAGCTCGTCAGCGG-3', and for the W45M mutation, the primers used were 5'-ATCGAGGGCTTTGGCAAGGATATGGCTCACAAGACTTG-3'/5'-CAAGTCTTGTGAGCCATATCCTTGCCAAAGCCCTCGAT-3'. For the double mutation F6LW45M, the plasmid containing the successful mutation for W45M was used as a template for the introduction of the second mutation using the same set of primers for the point mutation F6L. The mutations were introduced following the NZYMutagenesis kit (NZYTech) protocol using as template the pCSGmet2902 plasmid (27) containing the *ppcA* gene from *G. metallireducens*. The presence of desired mutations was confirmed by DNA sequencing in both strands by STAB VIDA.

Overexpression of ^{15}N-labeled and natural abundance cytochromes

The mutated proteins' expression and purification protocols followed that of wildtype PpcA, described by Portela *et al.* (23). Briefly, competent *Escherichia coli* BL21(DE3) cells harboring the plasmid pEC86 were transformed with 50 ng of pCSGmet2902 plasmid containing the desired mutation(s) and resistance to ampicillin. Cells were grown in liquid 2xYT medium supplemented with 100 μg/ml of ampicillin (NZYTech), 34 μg/ml of chloramphenicol (NZYTech) until they reached an absorbance between 1.5 and 1.8 at 600 nm. For the overexpression of natural abundance protein, protein overexpression was induced with a final concentration of 100 μM of IPTG (NZYTech), and cells were incubated overnight at 30 °C, 160 rpm. For the overexpression of ^{15}N-labeled protein, upon reaching an absorbance between 1.5 and 1.8 at 600 nm, cells were collected by centrifugation, washed twice with 250 ml of salt solution 1× M9, and then transferred to minimal medium M9 (in a ratio of 250 ml of minimal medium for each liter of 2xYT medium) supplemented with 100 μM $FeSO_4 \cdot 7H_2O$ (Merck), 1 mM δ-aminolevulinic acid (Merck), 4 mg/l D-glucose (VWR Chemicals), and 1 mg/l $^{15}NH_4Cl$ (Cambridge Isotope Laboratories [CIL]). After 90 min of incubation, protein expression was induced with a final concentration of 100 μM IPTG, and cells were grown overnight at 30 °C, 160 rpm.

For both overexpression protocols, cells were harvested by centrifugation, and the periplasmic fraction was isolated using lysis buffer containing 200 mM Tris–HCl (NZYTech), pH 8, 0.2 mM EDTA (Amresco), 20% sucrose (VWR Chemicals), and 0.5 mg/ml of lysozyme (Fluka). After centrifugation, the red supernatant was ultracentrifuged and then dialyzed twice in 10 mM Tris–HCl, pH 8 buffer.

Protein purification encompassed first a cation exchange chromatography step using 2 × 5 ml Bio-Scale Mini UNOsphere S Cartridges (BioRad) equilibrated in the same dialysis buffer and a second step using a Hiload 16/60 Superdex 75 column (GE Healthcare), equilibrated with 100 mM sodium phosphate buffer, pH 8.

The protein purity was evaluated by SDS-PAGE gel (5% acrylamide stacking gel and 15% acrylamide running gel) stained with BlueSafe (NZYTech).

Redox titrations followed by UV–visible spectroscopy

The redox titrations of PpcAF6L, PpcAW45M, and PpcAF6LW45M mutants were followed by UV–visible spectroscopy inside an anaerobic LABstar glove box (MBraun) with argon circulation and oxygen levels kept under 0.5 ppm, as previously described for the wildtype protein (23). The UV–visible spectra were acquired with a Thermo Scientific Evolution 300 UV–Visible spectrophotometer, and the sample temperature was maintained at 15 °C by using an external circulating bath. Solutions containing 10 μM of protein were prepared in 80 mM phosphate buffer with NaCl (250 mM final ionic strength) either at pH 7 or 8. The reduction potential value of the solution was measured using a combined Pt/Ag/AgCl electrode (Crison), calibrated at each titration with freshly prepared saturated solutions of quinhydrone (Merck) at pH 7 and 4 and checked at the end for stability. In order to ensure a good equilibrium between the redox centers and the working electrode, a mixture of the following redox mediators was added to the protein solution, all with approximately 2 μM final concentration: gallocyanine ($E^{0'}$ = +21 mV), methylene blue ($E^{0'}$ = +11 mV), indigo tetrasulfonate ($E^{0'}$ = −30 mV), indigo trisulfonate ($E^{0'}$ = −70 mV), indigo disulfonate ($E^{0'}$ = −110 mV), 2-hydroxy-1,4-naphthoquinone ($E^{0'}$ = −152 mV), anthraquinone-2,6-disulfonate ($E^{0'}$ = −184 mV), anthraquinone-2-

sulfonate ($E^{0'}$ = −225 mV), safranine O ($E^{0'}$ = −280 mV), neutral red ($E^{0'}$ = −325 mV), benzyl viologen ($E^{0'}$ = −345 mV), diquat ($E^{0'}$ = −350 mV), and methyl viologen ($E^{0'}$ = −440 mV). Each titration was performed at least two times both in the oxidative and reductive directions to check for hysteresis and reproducibility using sodium dithionite (Thermo Fisher Scientific) as reducing agent and potassium ferricyanide (Merck) as oxidizing agent. The reduced fraction of protein was determined by integrating the area of the α-peak (552 nm) above the line connecting the flanking isosbestic points (545 and 560 nm) to subtract the optical contribution of the redox mediators.

NMR studies

All NMR experiments were carried out on a Bruker Avance 600 MHz spectrometer equipped with a triple-resonance cryoprobe (TCI).

NMR experiments were carried out in the reduced state to evaluate the impact of the replacements on the global fold and heme core of the proteins. For these experiments, samples containing approximately 0.8 mM of protein were prepared in 45 mM sodium phosphate buffer with NaCl (100 mM final ionic strength), pH 7.1, either in 92% H_2O/8% ^2H_2O to assist the assignment of the mutants' backbone amide signals, or in ^2H_2O (99% atom) for the assignment of the mutants' heme substituent signals. For samples prepared in ^2H_2O, the protein was previously lyophilized twice and suspended in the appropriate buffer prepared exclusively on ^2H_2O (CIL isotopes). Similarly to the wildtype protein, 1D ^{1}H-NMR spectra were acquired before and after the lyophilization process for each mutant to confirm the integrity of the proteins. To fully reduce the samples, the NMR tubes were first sealed with a gas-tight serum cap, and the air was flushed out to avoid sample reoxidation. Reduction was achieved in the presence of gaseous hydrogen and catalytic amounts of hydrogenase from *Desulfovibrio vulgaris* (Hildenborough), as previously described (26). The pH of the samples was adjusted prior to its reduction using small amounts of NaO^{2}H or ^{2}HCl and was confirmed after the reduction in an anaerobic LABstar glovebox (MBraun). For the assignment of the heme substituent signals in the reduced state, 2D ^{1}H,^{1}H-TOCSY (60 ms) and 2D ^{1}H,^{1}H-NOESY (80 ms) in ^2H_2O were acquired. For backbone amide signal attribution in the reduced state, 2D ^{1}H,^{1}H-TOCSY (60 ms), 2D ^{1}H,^{1}H-NOESY (80 ms), and 2D ^{1}H,^{15}N-HSQC spectra were acquired. In both cases, the TOCSY and NOESY spectra were acquired with 2048 (t_2) × 512 (t_1) data points to cover a spectral width of 8.42 kHz, with 128 scans per increment. The 2D ^{1}H,^{15}N-HSQC spectra were acquired with 2048 (t_2) × 128 (t_1) data points to cover a spectral width of 8.42 kHz in ^{1}H and 4.87 kHz in ^{15}N with 160 scans per increment. For comparison with the NMR data obtained for the wildtype cytochrome, all experiments were carried out at 25 °C.

The samples for the NMR redox titrations were prepared with 80 μM of protein in 80 mM sodium phosphate buffer prepared in pure ^2H_2O (CIL isotopes), at six pH values (between 6.1 and 8.5), with NaCl (250 mM final ionic strength). The samples were fully reduced following the procedure indicated previously and partially oxidized by first removing the hydrogen from the sample with argon and then by introducing controlled amounts of air with a Hamilton syringe. The NMR redox titrations for observation of the stepwise oxidation of the protein followed the same procedure described for the wildtype protein (24). The oxidation patterns of the same set of heme methyls used for the wildtype cytochrome were monitored by 2D ^{1}H,^{1}H-EXSY spectra at 15 °C. The 2D ^{1}H,^{1}H-EXSY spectra were acquired with a mixing time of 25 ms, collecting 2048 (t_2) × 256 (t_1) data points to cover a sweep width of 27.6 kHz, with 256 scans per increment. 1D ^{1}H-NMR spectra were acquired before and after each 2D ^{1}H, ^{1}H-EXSY spectrum to ensure the maintenance of the oxidation state of the sample.

The assignment of the NMR signals was obtained as described for the wildtype protein (23, 24). ^{1}H chemical shifts were referenced to 2,2-dimethyl-2-silapentane-5-sulphonate at 0 ppm, and ^{15}N chemical shifts were calibrated through indirect referencing (28). The NMR spectra were processed using TOPSPIN software (Bruker Biospin) and analyzed with Sparky software (T. D. Goddard and D. G. Kneller; Sparky 3).

Thermodynamic model

In the present work, the thermodynamic characterization of the mutant PpcAW45M followed the same methodology employed to characterize the wildtype protein (24). This methodology was described in detail in the wildtype study and here is briefly summarized for clarity.

In a triheme cytochrome, four different redox stages coexist in solution as a consequence of the three consecutive one-electron transfer reversible steps that convert the fully reduced state (stage 0, S_0) in the fully oxidized state (stage 3, S_3) (Fig. S1). Each stage contains the microstates with the same number of oxidized hemes and, in addition, for each microstate, the protonable center(s) in the protein that modulate the hemes' reduction potential (redox–Bohr effect) can be protonated or deprotonated, leading to a minimum of 16 possible microstates (Fig. S1). Due to the close spatial disposition of the heme groups within the protein (23), the reduction potential of each heme is modulated by the oxidation stage of its neighbor (redox interactions) and by the pH solution (redox–Bohr interactions). Thus, the energy of each microstate is described in the full range of pH and solution potential as a sum of ten parameters: three reduction potentials, one pK_a of the redox–Bohr center, three redox interactions, and three redox–Bohr interactions. When the interconversion between microstates within the same oxidation stage—intramolecular electron exchange—is fast on the NMR timescale, and the interconversion between microstates of different oxidation stages—intermolecular electron exchange—is slow, the individual heme signals in the different oxidation stages can be discriminated in 2D ^{1}H, ^{1}H-EXSY NMR spectra. Moreover, the NMR paramagnetic

shifts caused by the oxidation of a particular heme are proportional to its degree of oxidation and, therefore, can be used to monitor its oxidation profile. The heme methyl NMR signal resonances are easily identifiable in the NMR spectra since their largest paramagnetic shifts move the signals to less crowded regions of the spectra at low field, making them the ideal candidates for probing the stepwise oxidation of the hemes throughout the redox titration. In order to determine the absolute potentials of the hemes, the information of the NMR redox titrations—indicating the relative heme reduction potentials and heme redox interactions—has to be complemented with the determination of the total reduced protein fraction through redox titrations followed by UV–visible spectroscopy. Just like for the wildtype protein, the NMR chemical shifts of the heme methyls $2^1CH_3^I$, $12^1CH_3^{III}$, and $2^1CH_3^{IV}$ were monitored through each oxidation stage, in 2D ^{1}H, ^{1}H-EXSY NMR spectra, in a pH range of 6.1 to 8.5 and then fitted simultaneously with UV–visible redox titrations performed at pH 7 and 8. The experimental uncertainty was evaluated from the line width of each NMR signal at half height, and an uncertainty of 3% was given to the UV–visible data points of the total optical signal.

Data availability

Both backbone and heme substituent signals were deposited in the Biological Magnetic Resonance Data Bank under accession numbers 50730 (for PpcAF6L data), 50731 (for PpcAW45M data), and 50732 (for PpcAF6LW45M data). All remaining data are contained within the article.

Supporting information—This article contains supporting Fig. S1, which was adapted from Ref. (29).

Author contributions—P.C.P. and C.A.S. designed the study; P.C.P., M.A.S., and L.R.T. prepared the samples. P.C.P., M.A.S., and C.A.S. acquired the NMR experiments and analyzed and treated the data. P.C.P. and C.A.S. wrote the manuscript. All authors approved the final version of the manuscript for submission.

Funding and additional information—This work was supported by Fundação para a Ciência e Tecnologia (FCT, Portugal) through the following grants: PTDC/BIA-BQM/31981/2017 (to C. A. S.) and 2020.04717.BD (to P. C. P.). This work was also supported by the Applied Molecular Biosciences Unit—UCIBIO, which is financed by national funds from FCT (UIDP/04378/2020 and UIDB/04378/2020). The NMR spectrometers at FCT NOVA are part of the National NMR Network (Portuguese Nuclear Magnetic Resonance Network) and are supported by FCT-MCTES (ROTEIRO/0031/2013—PINFRA/22161/2016) cofunded by FEDER through COMPETE 2020, Operational Program of Science and Innovation (Programa Operacional Ciência e Inovação), and Operational Regional Program of Lisbon (Programa Operacional Regional de Lisboa) and FCT through Central Administration Program of Investement and Development Expenses (Programa de Investimentos e Despesas de Desenvolvimento da Administração Central).

Conflict of interest—The authors declare that they have no conflicts of interest with the contents of this article.

Abbreviations—The abbreviations used are: CIL, Cambridge Isotope Laboratories; EXSY, EXchange SpectroscopY; HSQC, heteronuclear single quantum coherence.

References

1. Madigan, M., Martinko, J., Bender, K., Buckley, D., and Stahl, D. (2014) *Brock Biology of Microorganisms*, 14th Ed, Benjamin Cummings, Boston, MA
2. Lovley, D. R., Ueki, T., Zhang, T., Malvankar, N. S., Shrestha, P. M., Flanagan, K. A., Aklujkar, M., Butler, J. E., Giloteaux, L., Rotaru, A.-E., Holmes, D. E., Franks, A. E., Orellana, R., Risso, C., and Nevin, K. P. (2011) *Geobacter*: The microbe electric's physiology, ecology, and practical applications. *Adv. Microb. Physiol.* **59**, 1–100
3. Lovely, D. R. (1995) Microbial reduction of iron, manganese, and other metals. *Adv. Agron.* **54**, 175–231
4. Lovley, D. R., and Phillips, E. J. (1986) Organic matter mineralization with reduction of ferric iron in anaerobic sediments. *Appl. Environ. Microbiol.* **51**, 683–689
5. Aklujkar, M., Krushkal, J., DiBartolo, G., Lapidus, A., Land, M. L., and Lovley, D. R. (2009) The genome sequence of *Geobacter metallireducens*: Features of metabolism, physiology and regulation common and dissimilar to *Geobacter sulfurreducens*. *BMC Microbiol.* **9**, 109
6. Liu, G., Zhou, J., Chen, C., Wang, J., Jin, R., and Lv, H. (2013) Decolorization of azo dyes by *Geobacter metallireducens*. *Appl. Microbiol. Biotechnol.* **97**, 7935–7942
7. Ortiz-Bernad, I., Anderson, R. T., Vrionis, H. A., and Lovley, D. R. (2004) Vanadium respiration by *Geobacter metallireducens*: Novel strategy for *in situ* removal of vanadium from groundwater. *Appl. Environ. Microbiol.* **70**, 3091–3095
8. Lloyd, J. R., Sole, V. A., Van Praagh, C. V., and Lovley, D. R. (2000) Direct and Fe(II)-mediated reduction of technetium by Fe(III)-reducing bacteria. *Appl. Environ. Microbiol.* **66**, 3743–3749
9. Reguera, G., and Kashefi, K. (2019) The electrifying physiology of *Geobacter* bacteria, 30 years on. *Adv. Microb. Physiol.* **74**, 1–96
10. Santoro, C., Arbizzani, C., Erable, B., and Ieropoulos, I. (2017) Microbial fuel cells: From fundamentals to applications. A review. *J. Power Sources* **356**, 225–244
11. Butler, J. E., Young, N. D., and Lovley, D. R. (2010) Evolution of electron transfer out of the cell: Comparative genomics of six *Geobacter* genomes. *BMC Genomics* **11**, 40
12. Dantas, J. M., Morgado, L., Aklujkar, M., Bruix, M., Londer, Y., Schiffer, M., Pokkuluri, P. R., and Salgueiro, C. A. (2015) Rational engineering of *Geobacter sulfurreducens* electron transfer components: A foundation for building improved *Geobacter*-based bioelectrochemical technologies. *Front. Microbiol.* **6**, 752
13. Salgueiro, C. A., and Dantas, J. M. (2016) Multiheme cytochromes. In *Multiheme Cytochromes*, Springer Berlin Heidelberg, Berlin, Heidelberg: 1–39
14. Zacharoff, L., Chan, C. H., and Bond, D. R. (2016) Reduction of low potential electron acceptors requires the CbcL inner membrane cytochrome of *Geobacter sulfurreducens*. *Bioelectrochemistry* **107**, 7–13
15. Levar, C. E., Chan, C. H., Mehta-Kolte, M. G., and Bond, D. R. (2014) An inner membrane cytochrome required only for reduction of high redox potential extracellular electron acceptors. *mBio* **5**, 1–9
16. Liu, Y., Wang, Z., Liu, J., Levar, C., Edwards, M. J., Babauta, J. T., Kennedy, D. W., Shi, Z., Beyenal, H., Bond, D. R., Clarke, T. A., Butt, J. N., Richardson, D. J., Rosso, K. M., Zachara, J. M., *et al.* (2014) A trans-outer membrane porin-cytochrome protein complex for extracellular electron transfer by *Geobacter sulfurreducens* PCA. *Environ. Microbiol. Rep.* **6**, 776–785
17. Wang, F., Gu, Y., O'Brien, J. P., Yi, S. M., Yalcin, S. E., Srikanth, V., Shen, C., Vu, D., Ing, N. L., Hochbaum, A. I., Egelman, E. H., and Malvankar,

N. S. (2019) Structure of microbial nanowires reveals stacked hemes that transport electrons over micrometers. *Cell* **177**, 361–369.e310
18. Tan, Y., Adhikari, R. Y., Malvankar, N. S., Ward, J. E., Woodard, T. L., Nevin, K. P., and Lovley, D. R. (2017) Expressing the *Geobacter metallireducens* PilA in *Geobacter sulfurreducens* yields pili with exceptional conductivity. *mBio* **8**, 1–9
19. Yalcin, S. E., O'Brien, J. P., Gu, Y., Reiss, K., Yi, S. M., Jain, R., Srikanth, V., Dahl, P. J., Huynh, W., Vu, D., Acharya, A., Chaudhuri, S., Varga, T., Batista, V. S., and Malvankar, N. S. (2020) Electric field stimulates production of highly conductive microbial OmcZ nanowires. *Nat. Chem. Biol.* **16**, 1136–1142
20. Tremblay, P.-L., Aklujkar, M., Leang, C., Nevin, K. P., and Lovley, D. (2012) A genetic system for *Geobacter metallireducens*: Role of the flagellin and pilin in the reduction of Fe(III) oxide. *Environ. Microbiol. Rep.* **4**, 82–88
21. Pessanha, M., Morgado, L., Louro, R. O., Londer, Y. Y., Pokkuluri, P. R., Schiffer, M., and Salgueiro, C. A. (2006) Thermodynamic characterization of triheme cytochrome PpcA from *Geobacter sulfurreducens*: evidence for a role played in e-/H+ energy transduction. *Biochemistry* **45**, 13910–13917
22. Ferreira, M. R., Dantas, J. M., and Salgueiro, C. A. (2018) The triheme cytochrome PpcF from *Geobacter metallireducens* exhibits distinct redox properties. *FEBS Open Bio* **8**, 1897–1910
23. Portela, P. C., Fernandes, T. M., Dantas, J. M., Ferreira, M. R., and Salgueiro, C. A. (2018) Biochemical and functional insights on the triheme cytochrome PpcA from *Geobacter metallireducens*. *Arch. Biochem. Biophys.* **644**, 8–16
24. Fernandes, T. M., Morgado, L., and Salgueiro, C. A. (2018) Thermodynamic and functional characterization of the periplasmic triheme cytochrome PpcA from *Geobacter metallireducens*. *Biochem. J.* **475**, 2861–2875
25. Pessanha, M., Londer, Y. Y., Long, W. C., Erickson, J., Pokkuluri, P. R., Schiffer, M., and Salgueiro, C. A. (2004) Redox characterization of *Geobacter sulfurreducens* cytochrome c_7: Physiological relevance of the conserved residue F15 probed by site-specific mutagenesis. *Biochemistry* **43**, 9909–9917
26. Morgado, L., Bruix, M., Orshonsky, V., Londer, Y. Y., Duke, N. E. C., Yang, X., Pokkuluri, P. R., Schiffer, M., and Salgueiro, C. A. (2008) Structural insights into the modulation of the redox properties of two *Geobacter sulfurreducens* homologous triheme cytochromes. *Biochim. Biophys. Acta Bioenerg.* **1777**, 1157–1165
27. Londer, Y. Y., Pokkuluri, P. R., Tiede, D. M., and Schiffer, M. (2002) Production and preliminary characterization of a recombinant triheme cytochrome c_7 from *Geobacter sulfurreducens* in *Escherichia coli*. *Biochim. Biophys. Acta Bioenerg.* **1554**, 202–211
28. Wishart, D. S., Bigam, C. G., Yao, J., Abildgaard, F., Dyson, H. J., Oldfield, E., Markley, J. L., and Sykes, B. D. (1995) ^{1}H, ^{13}C and ^{15}N chemical shift referencing in biomolecular NMR. *J. Biomol. NMR* **6**, 135–140
29. Dantas, J. M., Portela, P. C., Fernandes, A. P., Londer, Y. Y., Yang, X., Duke, N. E. C., Schiffer, M., Pokkuluri, P. R., and Salgueiro, C. A. (2019) Structural and functional relevance of the conserved residue V13 in the triheme cytochrome PpcA from *Geobacter sulfurreducens*. *J. Phys. Chem. B* **123**, 3050–3060
30. Altschul, S. F., Gish, W., Miller, W., Myers, E. W., and Lipman, D. J. (1990) Basic local alignment search tool. *J. Mol. Biol.* **215**, 403–410
31. Schumann, F. H., Riepl, H., Maurer, T., Gronwald, W., Neidig, K.-P., and Kalbitzer, H. R. (2007) Combined chemical shift changes and amino acid specific chemical shift mapping of protein–protein interactions. *J. Biomol. NMR* **39**, 275–289
32. Morgado, L., Bruix, M., Pessanha, M., Londer, Y. Y., and Salgueiro, C. A. (2010) Thermodynamic characterization of a triheme cytochrome family from *Geobacter sulfurreducens* reveals mechanistic and functional diversity. *Biophys. J.* **99**, 293–301